NASA/TM–20210021870

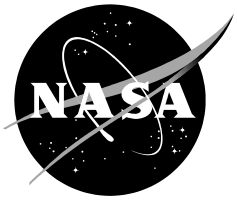

Tiltrotor Test Rig Aerodynamic Tares

C. W. Acree, Jr.
Ames Research Center
Moffett Field, California

December 2021

NASA STI Program Report Series

The NASA STI Program collects, organizes, provides for archiving, and disseminates NASA's STI. The NASA STI program provides access to the NTRS Registered and its public interface, the NASA Technical Reports Server, thus providing one of the largest collections of aeronautical and space science STI in the world. Results are published in both non-NASA channels and by NASA in the NASA STI Report Series, which includes the following report types:

- TECHNICAL PUBLICATION. Reports of completed research or a major significant phase of research that present the results of NASA Programs and include extensive data or theoretical analysis. Includes compilations of significant scientific and technical data and information deemed to be of continuing reference value. NASA counterpart of peer-reviewed formal professional papers but has less stringent limitations on manuscript length and extent of graphic presentations.

- TECHNICAL MEMORANDUM. Scientific and technical findings that are preliminary or of specialized interest, e.g., quick release reports, working papers, and bibliographies that contain minimal annotation. Does not contain extensive analysis.

- CONTRACTOR REPORT. Scientific and technical findings by NASA-sponsored contractors and grantees.

- CONFERENCE PUBLICATION. Collected papers from scientific and technical conferences, symposia, seminars, or other meetings sponsored or co-sponsored by NASA.

- SPECIAL PUBLICATION. Scientific, technical, or historical information from NASA programs, projects, and missions, often concerned with subjects having substantial public interest.

- TECHNICAL TRANSLATION. English-language translations of foreign scientific and technical material pertinent to NASA's mission.

Specialized services also include organizing and publishing research results, distributing specialized research announcements and feeds, providing information desk and personal search support, and enabling data exchange services.

For more information about the NASA STI program, see the following:

- Access the NASA STI program home page at http://www.sti.nasa.gov

- Help desk contact information:

https://www.sti.nasa.gov/sti-contact-form/
and select the "General" help request type.

NASA/TM–20210021870

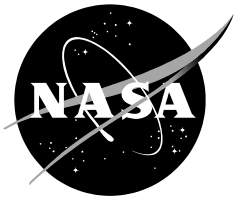

Tiltrotor Test Rig Aerodynamic Tares

C. W. Acree, Jr.
Ames Research Center
Moffett Field, California

National Aeronautics and
Space Administration

Ames Research Center
Moffett Field, California 94035-1000

December 2021

ACKNOWLEDGMENTS

The author wishes to thank Tom Norman (NASA Ames Research Center) for his invaluable advice born out of deep experience in wind-tunnel testing, and Ethan Romander (also NASA) for maintaining the TTR/699 database under the demands of countless revisions.

Available from:

NASA STI Support Services
Mail Stop 148
NASA Langley Research Center
Hampton, VA 23681-2199
757-864-9658

National Technical Information Service
5301 Shawnee Road
Alexandria, VA 22312
webmail@ntis.gov
703-605-6000

This report is also available in electronic form at

http://ntrs.nasa.gov

TABLE OF CONTENTS

NOMENCLATURE

NFAC	National Full-Scale Aerodynamics Complex
TTR	Tiltrotor Test Rig

q	Dynamic pressure, $\frac{1}{2}\rho V^2$
se_q	Standard error of fit to q
T	Wind tunnel air temperature
V	Wind tunnel airspeed
Ω	Rotor shaft speed
ρ	Atmospheric density
s	Standard deviation
Ψ	Wind-tunnel yaw angle

Balance and Shaft Loads

AF	Axial Force
NF	Normal Force
SF	Side Force
PM	Pitching Moment
RM	Rolling Moment
YM	Yaw Moment
B3, B4	Loads from B3 & B4 calibrations
_SH	Shaft Loads
_A, _B	Primary & backup strain gages

TILTROTOR TEST RIG AERODYNAMIC TARES

C. W. Acree, Jr.

Ames Research Center

SUMMARY

The Tiltrotor Test Rig (TTR) is a NASA facility designed to test full-scale proprotors in the National Full-Scale Aerodynamics Facility (NFAC). The first wind-tunnel entry included measurements of aerodynamic loads (tares) on the spinner without a rotor. The TTR has an onboard balance for direct measurement of rotor loads, so these tares comprise only spinner loads. Spinner tares also affect shaft loads measured independently of the balance. The results show that in axial flow, spinner drag is a linear function of dynamic pressure as expected, but at other flow angles, spinner loads include substantial lift and drag. Furthermore, there is a pronounced Magnus effect when the spinner is sideways to the flow. There is a sharp change in aerodynamic load at 90-deg yaw angle, indicating separation. Equations were developed to characterize the spinner tares at any arbitrary combination of yaw angle and airspeed.

INTRODUCTION

The Tiltrotor Test Rig (TTR) is designed to test large-scale proprotors in high-speed axial flight up to 300 knots and tiltrotor conversion mode up to 180 knots. The TTR can also test in helicopter mode up to 120 knots. The first entry of the TTR into the National Full-Scale Aerodynamics Complex (NFAC) was completed in November 2018. Development of the TTR is described in Ref. 1, and the test program is described in Refs. 2-4.

The purpose of this report is to document the recommended TTR spinner aerodynamic tare equations. The requirement is to develop mathematical models for each force and moment that adequately capture the nonlinear aerodynamic loads (tares) on the spinner without the rotor installed. Estimates of isolated rotor loads can then be made by subtracting the loads predicted by the model from data taken with the rotor installed.

Rotor loads are measured by a dedicated balance. In addition, the rotor shaft has strain gages to check that loads remain within structural limits. Both sets of loads are affected by spinner tares. Separate sets of equations for spinner tares were developed for balance and shaft loads. This report focusses primarily on the balance.

Extreme nonlinearity at 90-deg yaw (Ψ) forces the use of multiple equations, each for a different range of yaw angles. Airplane-mode and helicopter-mode data overlap below 160 knots, so care must be taken to apply only one set of corrections.

Discussion begins with a general overview of the TTR configuration used for aerodynamic tares, followed by separate sections for aerodynamic tares in each load axis. Normal force (drag) is divided into low- and high-speed sections. Torque requires no tare corrections, as will be

explained. Spinner tares derived from the rotor balance and rotor shaft strain gages are described separately. Appendix A presents tare data with exposed hub yokes.

The TTR rotor balance has two independent sets of strain gages, each with its own set of calibration coefficients. By tradition, a set of strain gages and associated calibration coefficients is called a "balance" (not to be confused with the physical rotor balance; the distinction will be made herein where necessary). The best of several such balances derived for the TTR are the "B3" and "B4" balances. Details are given in the next section. Neither balance provided good tare data for all loads at all conditions, so the tares were sometimes derived from only one of the balance outputs. Consequently, the aerodynamic tare equations are independent of the balance used. In contrast, tares derived from the shaft gages depend upon the particular set of measurements used. Appendix B lists detailed curve-fit parameters from which the tare equations were derived.

The effects of spinner pressure were determined to have negligible effect on aerodynamic tares. Details are given in Appendix C.

AERODYNAMIC TARE CONFIGURATION AND MEASUREMENT DESCRIPTION

Figures 1 and 2 show the spinner with and without blades installed, respectively. The forward dome and rotating skirt fairings together constitute the spinner. Aerodynamic tare data were taken with the openings for the blade shanks covered (Fig. 2). A third configuration used for only one data run is shown in Appendix A.

The proper setup for measuring spinner tares poses a dilemma, in that neither a blades-off nor hub-off configuration provides the exact flow conditions that would exist if the blades had no aerodynamic effect on the spinner. The hub yokes and bearings are covered by the blade roots, which act as aerodynamic fairings extending inside the spinner skirts (Fig. 1).

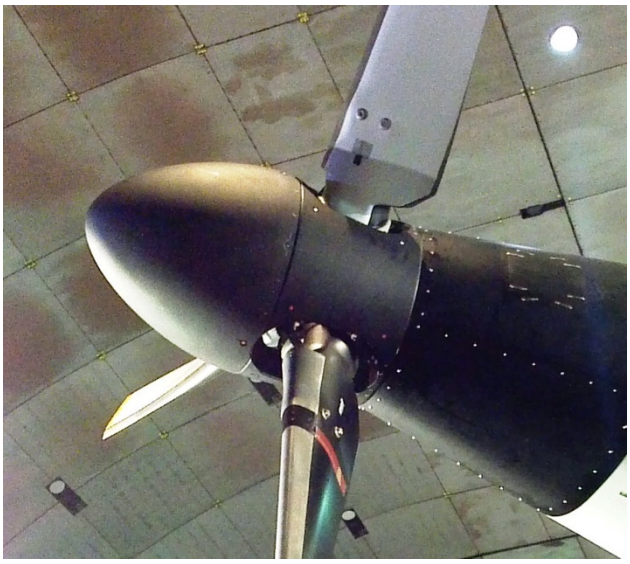

Fig. 1. TTR spinner with blades installed.

Fig. 2. TTR spinner and skirt fairings without blades, hole covers installed.

Removing the blades would expose the yokes flatwise to the flow and create high-drag flow conditions not present during normal operations. If instead the entire hub were to be removed, the flow disturbance caused by the yokes would not exist, but the effective area of the holes in the skirt fairings would be much larger than with blades installed, again resulting in non-representative flow conditions.

Given that there is no perfect way to acquire spinner tare data, an ideal spinner was simulated by removing the hub and covering the skirt holes. This is the cleanest possible configuration, hence the lowest spinner drag. It should also be the easiest configuration to model in Computational Fluid Dynamics (CFD). Figure 2 shows the fully-faired spinner.

TTR rotor and spinner loads are measured by two different systems. The primary system comprises a cylindrical balance and coaxial torque tube, collectively referred to as the rotor balance. Figure 3 shows the axis system used for the TTR rotor balance. Table 1 defines the load labels and polarities.

The vectors shown in Fig. 3 are referenced to the hub axis system, as appropriate for rotor performance data. However, standard NFAC practice is to apply aerodynamic tares in the balance axis system, which is offset 87.7 in aft of the hub. Only the moments PM and RM are affected by the different axis systems. All loads are given in the balance axis system unless noted otherwise. The balance is described in more detail in Ref. 1.

Nonrotating, zero-airspeed data were taken at the beginning and end of each run to establish reference points (“static” points). All balance data presented here have been corrected for thermal drift by interpolating any offsets between static points. Other temperature effects on NF tares are discussed in context.

For aerodynamic tares, balance torque YM arises almost entirely from bearing drag. It is presented herein only as a check on the reasonableness of the data.

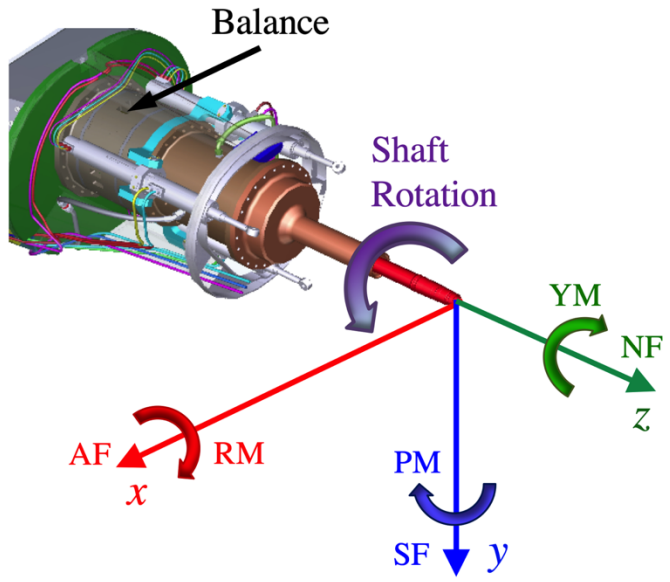

Fig. 3. TTR balance axis system, referenced to the rotor hub.

Table 1. Rotor Balance Load Definitions and Polarities

Load	Label	Axis	Positive Direction
Axial Force	AF	*x*	right
Side Force	SF	*y*	down
Normal Force (thrust)	NF	*z*	forward
Lateral Moment	RM	*x*	nose down
Normal Moment	PM	*y*	nose right
Torque	YM	*z*	opposite to rotation

For reference, Table 2 lists the calibration ranges and uncertainties ($\pm 2\sigma$ errors) for the B3 and B4 balance calibrations.

Table 2. Rotor Balance Calibration Ranges and Uncertainties

Hub Load	Range	B3 2σ Error	B3 2σ/Range	B4 2σ Error	B4 2σ/Range
Normal force, NF	15,148 lb	120 lb	0.80 %	137 lb	0.90 %
In-plane horizontal, AF	±8,250 lb	25 lb	0.15 %	24 lb	0.14 %
In-plane vertical, SF	±8,250 lb	18 lb	0.11 %	17 lb	0.11 %
Hub moment, vertical axis, PM	±7,500 ft-lb	175 ft-lb	1.16 %	179 ft-lb	1.19 %
Hub moment, horizontal, RM	±7,500 ft-lb	225 ft-lb	1.50 %	217 ft-lb	1.44 %
Torque, YM	22,338 ft-lb	93 ft-lb	0.42 %	93 ft-lb	0.41 %

The second system for measuring spinner and rotor loads utilizes multiple sets of rotating shaft strain gages calibrated for bending moment. Non-rotating hub loads are derived from orthogonal pairs of gages located at multiple locations along the shaft. The shaft gages were not intended for precision measurements, nor do they measure thrust or torque. The shaft gages were accordingly given only simple bench calibrations. The resulting error statistics are not comparable to those in Table 2 and are not discussed here.

DATA SUMMARY

The aerodynamic tare data were taken in May 2017. With the TTR in the 40- by 80-ft test section and all NFAC fan-drive blades installed, the minimum airspeed in NFAC Utility Mode was slightly under 60 knots. 60 knots was therefore chosen as the minimum airspeed for the tare runs to ensure enough margin to always maintain that airspeed. In practice, most minimum-speed tare data were taken at 61 knots.

The tare data for helicopter mode can be divided into several subsets, with coarse (15-deg) and fine (2-deg) increments in yaw angles at fixed airspeeds, and variations in airspeed at fixed yaw angles. The data acquired during yaw variations proved more useful for deriving low-speed tare corrections than the airspeed variations. High-speed tare data (airplane mode, >154 knots) were acquired and analyzed separately, as described in the section “NF Tares”.

In the discussion immediately following, trends for aerodynamic tares are presented using data derived from the rotor balance. Tare data for the rotor shaft strain gages are discussed in a separate section, later in this report.

Coarse yaw data are available at seven different airspeeds (61 to 154 knots, q=12 to 75 lb/ft^2; Figs. 4 and 5), but fine yaw data were taken at only three airspeeds (61, 105, and 154 knots, q=12, 36, and 75 lb/ft^2; Fig. 6). Figure 4 shows the test conditions for a subset of the tare data taken at coarse and fine increments of yaw angle and consistent values of dynamic pressure. Figure 5 presents balance data taken at the test conditions of Fig. 4. The dark vertical bars in Figs. 5 and 6 represent $\pm 2\sigma$ uncertainty (95% criterion) from the balance calibration (Table 2). (The bars represent calibration accuracies, not data point statistics, hence the nontraditional format.) All data shown in Fig. 5 are for the B3 balance.

The coarse yaw sweeps show consistent patterns of behavior at all airspeeds, but cannot properly capture the nonlinear behavior near 90-deg yaw (assumed to be caused by separation). Airspeed sweeps at fixed yaw reveal nothing about how loads vary near 90 deg, and the coarse yaw data are sufficiently consistent that airspeed sweeps contribute little additional insight (hence such data are not shown here). Therefore, low-speed tare corrections were derived exclusively from the fine-yaw data (Fig. 6), on the grounds that such data adequately represent the full range of aerodynamic characteristics while better revealing behavior near stall. Both coarse- and fine-yaw data are presented in the following sections.

Aside from YM, all loads plotted in Fig. 6 show sharp jumps in values at 90 deg yaw, thought to result from separation. In most cases, separation results in severe scatter at 90 deg, which causes problems for curve fitting. In particular, using a least-squares error criterion may not be viable when there is high scatter at a discrete value of the independent variable.

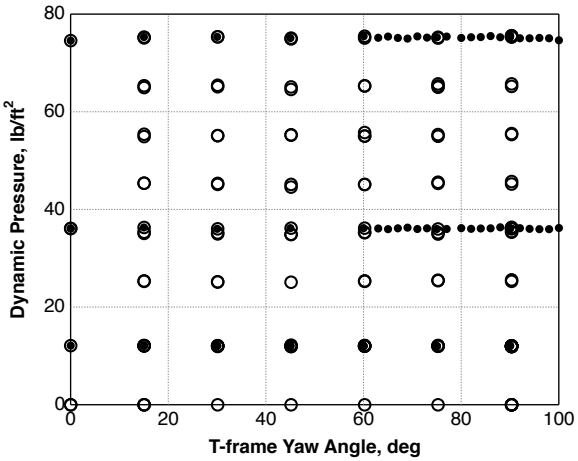

Fig. 4. Aero tare data subset: 569 rpm, constant q values, 15-deg and 2-deg yaw increments.

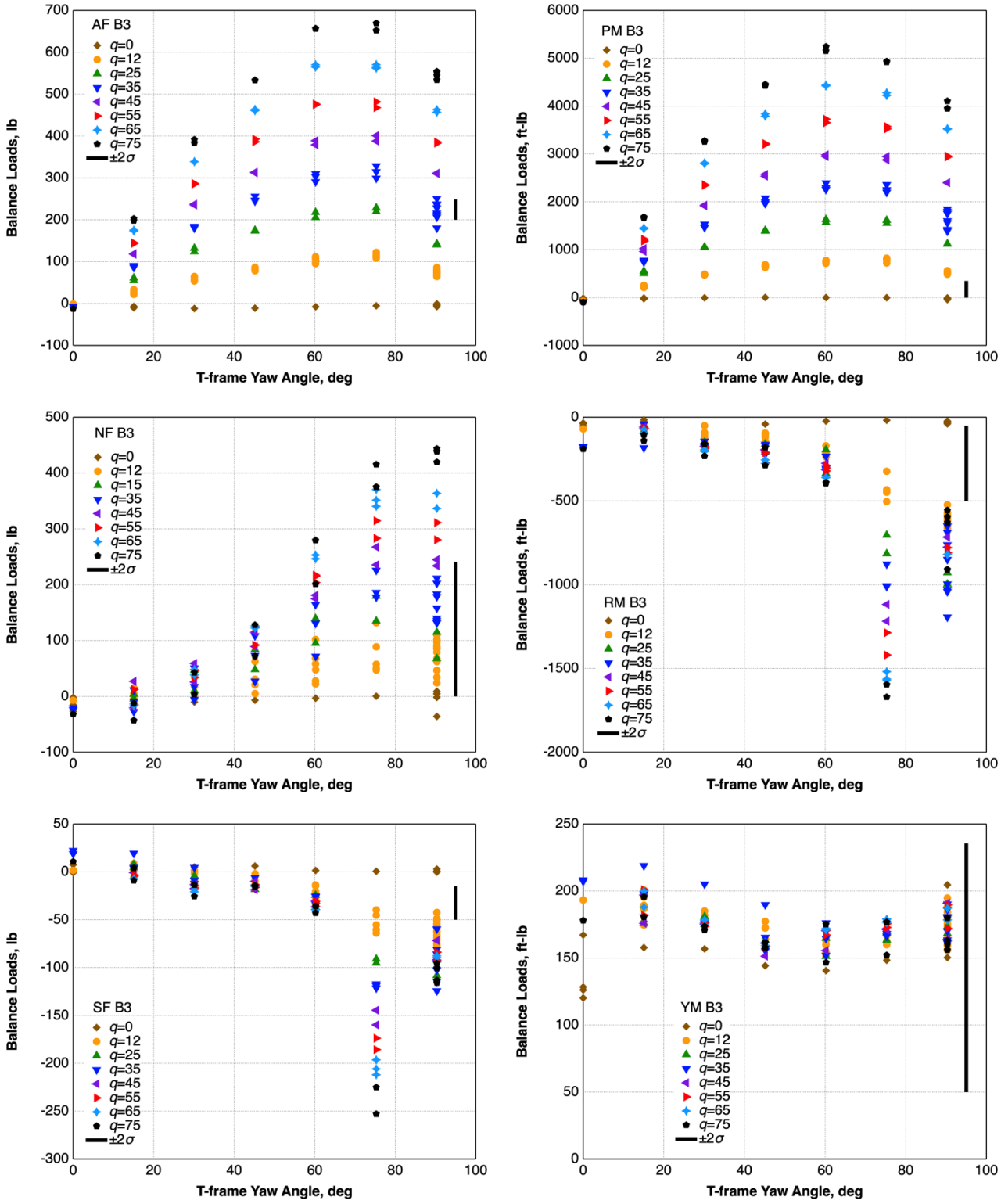

Fig. 5. Balance B3 tare variations with yaw angle, at the test conditions in Fig. 4.

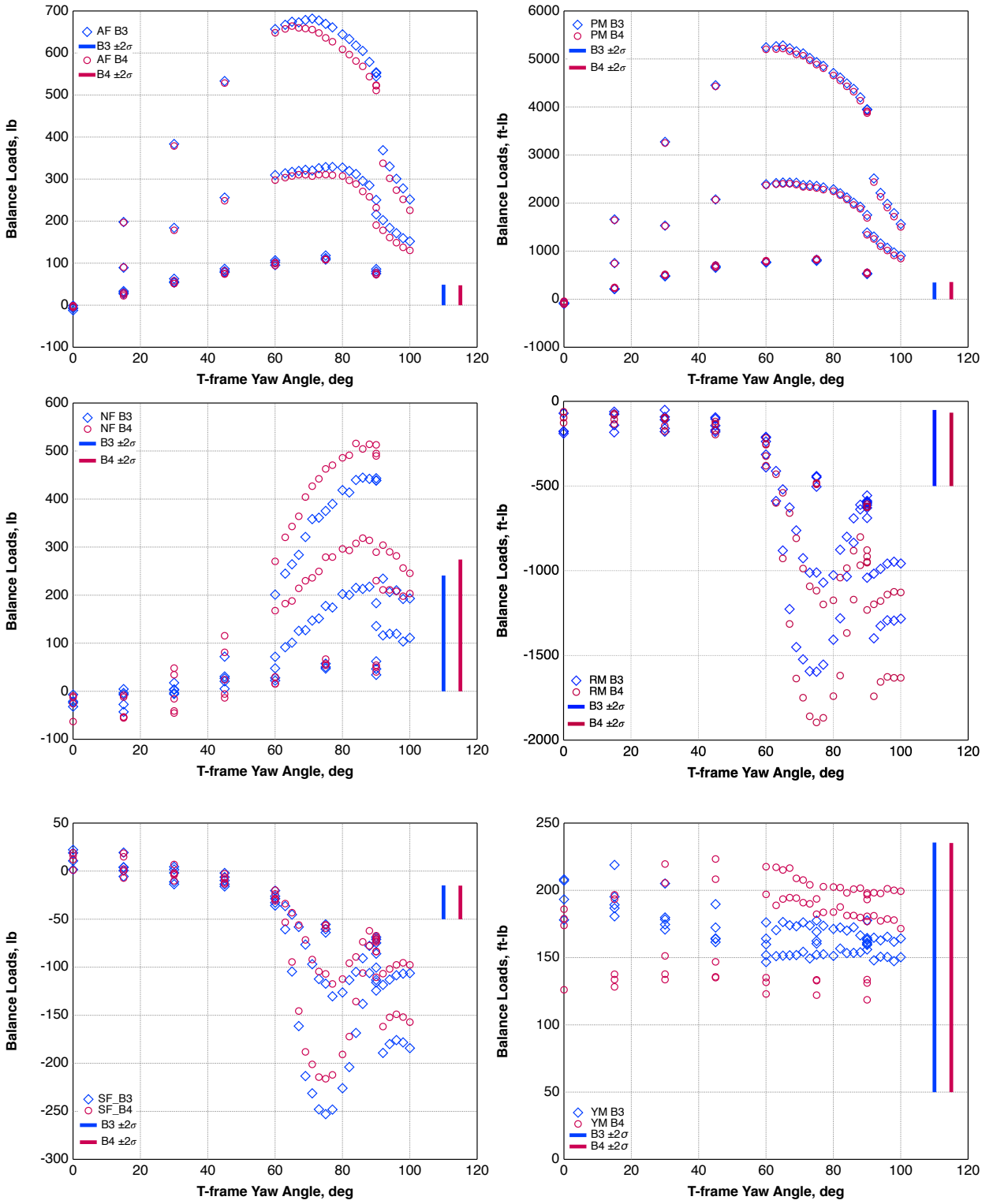

Fig. 6. B3 and B4 balance tare variations with yaw angle, at fine increments; q=12, 36, and 75 lb/ft2.

For aerodynamic tares, hub moments PM and RM in balance-centered axes are dominated by in-plane loads AF and SF, respectively. Hence PM responses are closely similar to AF, and RM is similar to SF, each with a change of scale corresponding to the change of units (force to moment). The aerodynamic center of pressure varies with yaw angle, so the moments do not match the forces point-by-point.

AF and PM have the most consistent responses between the two balances. NF, SF, and RM show generally consistent trends, but with offsets and/or different sensitivities for the balances. The YM tares, while showing offsets between the two balances, are small and vary little with yaw angle. These results confirm that the tare values of YM reflect bearing drag, not aerodynamics, so no aerodynamic tares are needed.

Additional data were taken with the blades removed and the hub yokes exposed. See Appendix A for figures and discussion.

INDIVIDUAL TARE CORRECTIONS FOR THE ROTOR BALANCE

Physically, all tares should equal zero at q=0 lb/ft^2, and all but NF should equal zero at Ψ=0 deg. However, the data do not always follow the expected behavior, assumed here to be caused by measurement errors such as hysteresis. There is also a desire to keep the tare corrections simple. These considerations lead to frequent use of engineering judgement and simplifying assumptions in the development of recommended tare corrections, as detailed in the following sections. Tares are defined only in the range $0 \le \Psi \le 110$ deg and the equations are not symmetric about zero. If aerodynamic tares are desired outside of this range, new equations will have to be developed, with due attention to polarity at negative Ψ.

Curve fits were made directly to loads data where possible, but the best results were sometimes obtained with fits to normalized load/q or load/V. In such cases, the curve fits were transformed back into standard units for plotting. All data but the high-speed NF tares were taken at helicopter-mode tip speed (569 rpm); the high-speed tares were taken at 478 rpm.

In the following figures with curve fits, individual points are loads data at actual yaw angles, and lines are predictions by the tare equations at arbitrary yaw angles.

AF Tares

In principle, AF tares should follow a q*A*sinΨ function and NF should follow a q*(B*sinΨ + C*cosΨ) function, where A, B, and C are coefficients to be determined. However, attempts to use such functions gave poor results at high yaw angles, so polynomial fits were used instead. Typically, higher order fits were needed below Ψ=90 deg than above, largely because the high scatter at 90 deg undermined any improvement at higher orders for Ψ>90.

Dividing AF by q collapses the data nicely, but still leaves a sharp drop at 90 deg Ψ (Fig. 7). To get good curve fits, the data at Ψ=90 deg were simply ignored, with different tare equations below and above 90 deg (Fig. 8):

Yaw ≤ 90, from 3rd-order curve fit to AF/q:
$AF\ tare\ (lb) = -2.26E{-}05q\Psi^3 + 1.40E{-}03q\Psi^2 + 0.140q\Psi - 0.0100q$

Yaw > 90, from 2nd-order curve fit to AF/q:
$AF\ tare\ (lb) = 8.49E{-}03q\Psi^2 - 1.81q\Psi + 99.3q$

The last term in the equation for yaw ≤ 90 (effect of q only) can be set to zero with negligible effect on accuracy (not visible at the scale of Fig. 8.)

Appendix B

lists the curve-fit parameters used to generate the coefficients in the equations above and the curves in Fig. 8 etc.

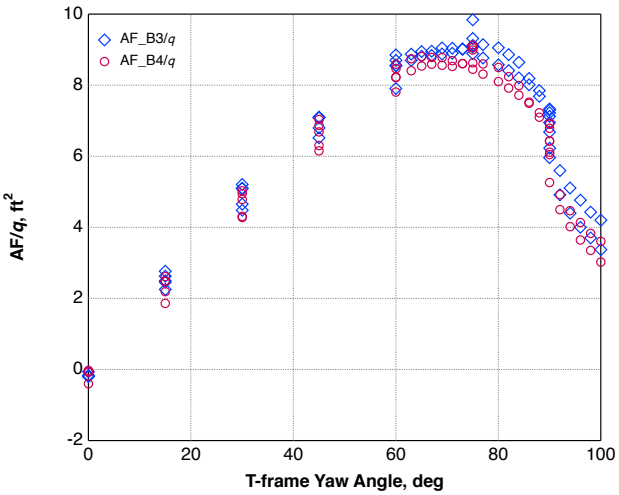

Fig. 7. AF/q tare data at three values of q.

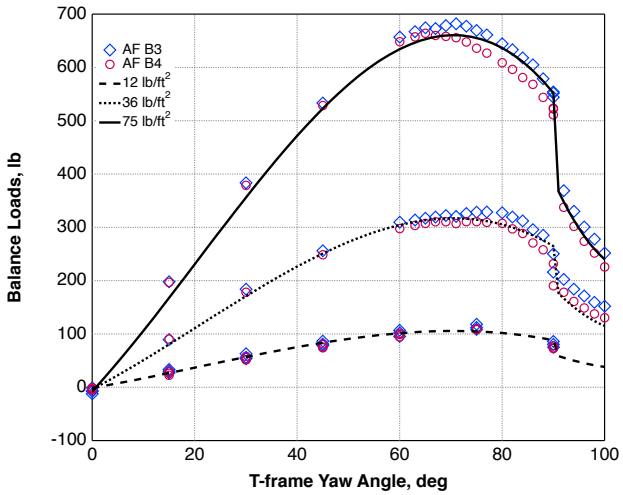

Fig. 8. Aero tare model for AF.

NF Tares

NF presented several unique problems. High-speed (airplane mode) data were taken only at zero yaw; only the low-speed data (<155 knots) includes yaw sweeps. The tare equations must transition smoothly between low- and high-speed conditions while preserving low-speed trends with yaw angle. Minimizing the sum-of-squares error proved insufficient, because the resulting equations overshot the data near 90 deg yaw, where helicopter-mode performance is critical. Considerable tuning of the tare equations was required to get acceptable behavior at both low and high speeds and at low and high yaw angles.

NF aerodynamic tares are discussed separately for low and high speeds.

Low-Speed NF Tares

Figure 9 shows that the B3 and B4 balances have different sensitivities and zero offsets for NF. Normalizing by q (Fig. 9) reveals that the B4 data are less consistent, particularly at low values of Ψ. Furthermore, NF/q should be less than 1 ft^2 at Ψ=0 deg, which is consistent with the B3 data but not B4. Therefore, only the B3 data were used to determine the NF aero tare corrections.

As with AF, there is a sharp drop at Ψ=90 deg. No curve fit gave good results at both 0 and 90 deg. To get an acceptable transition to high-speed NF tares, the data at Ψ=0 were excluded from the low-speed curve fits. The nonlinear curve fits are thus divided into two ranges, $0<\Psi<90$ and $\Psi\geq 90$ deg.

The results for the simplest useable fit to NF are shown in Fig. 10; the coefficients are given immediately below.

Yaw = 0, from high-speed data (see next section):
NF tare (lb) = $-0.833q$

0 < Yaw < 90, from 3rd-order curve fit to NF:
NF tare (lb) = $-2.21\text{E}{-05}q\Psi^3 + 3.79\text{E}{-03}q\Psi^2 - 9.47\text{E}{-02}q\Psi - 10.41$

Yaw > 90, from 2nd-order curve fit to NF:
NF tare (lb) = $-8.64\text{E}{-04}q\Psi^2 - 0.108q\Psi + 27.7$

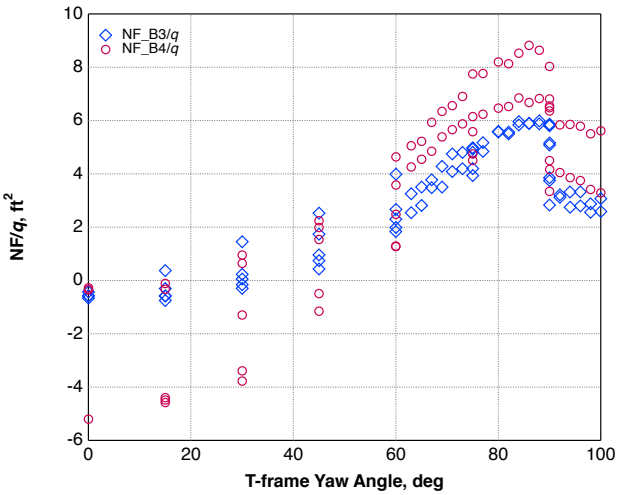

Fig. 9. NF/q tare data at three values of q.

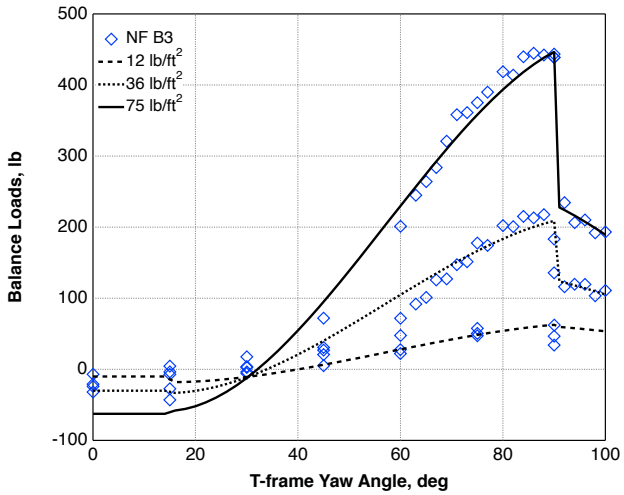

Fig. 10. Aero tare model for NF.

Although the errors in the 3rd-order fits to NF (Fig. 10) are less than the balance uncertainty, a failure to match the flattened trend above 80 deg yaw is evident, as are poor fits near 60 deg above minimum q. The transition from high-speed tares at 0 deg to low-speed tares at 15 deg and above is imperfect but acceptable. Obtaining a better match for Ψ>45 deg would require a 4th-order fit to NF and more elaborate equations from 0 to 15 deg. Given the magnitude of the $\pm 2\sigma$ uncertainty, more complicated equations than those provided here are difficult to justify.

A better fit at and above Ψ=90 deg could be achieved by inverting the problem and fitting Ψ to NF with a power-law or exponential function. Again, the additional complication is hard to justify given the uncertainty in the balance relative to the magnitude of the tares, and so is not recommended.

High-Speed NF Tares

Determining appropriate aerodynamic tares at high speed is severely complicated by (assumed) thermal drift and the small magnitude of the tares relative to the range of the rotor balance. Figure 11 shows the NF data for the B3 and B4 balances plotted against dynamic pressure q, here at zero yaw (Ψ=0). All data were taken at 478 rpm, as appropriate for airplane mode.

There appear to be two types of nonlinearity: (1) a low-speed effect wherein NF first increases, then decreases; the B4 data show this effect for both increasing and decreasing q, but B3 shows it only for increasing q; and (2) classic hysteresis above 50 lb/ft^2, evident in both balances. The B3 and B4 data have similar hysteresis above 50 lb/ft^2.

Figure 11 reveals that correcting the data for temperature effects by interpolating between static reference points was not fully effective. Dynamic pressure implicitly includes temperature, but Fig. 11 shows that this dynamic effect does not explain the hysteresis.

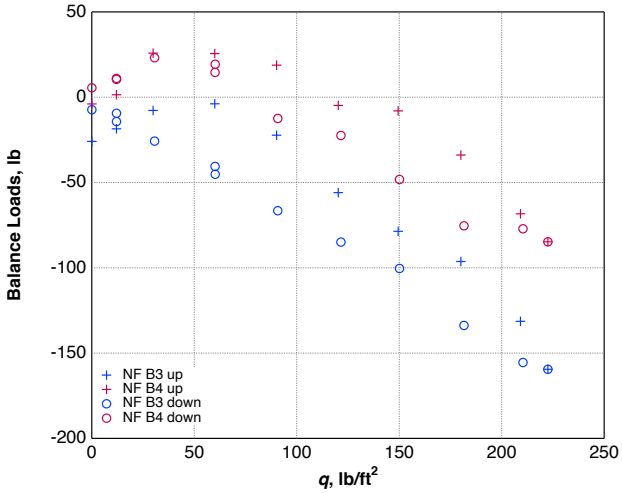

Fig. 11. Aerodynamic tare data for NF at high speed, yaw = 0, 478 rpm.

The following paragraphs discuss temperature effects in more detail. Temperatures used include the tunnel static temperature as well as temperature measurements on the rotor balance. The balance has extensive temperature measurements on both the metric and non-metric ends of the cylinder ("metric ring" and "ground ring").

Figures 12 and 13 plot different temperatures against dynamic pressure. The difference between average metric-ring and ground-ring temperatures (ΔT, Fig. 12) increases with q until about 50 lb/ft^2, then remains nearly constant and follows a similar trend as q decreases. Tunnel static temperature (TSF) shows a pronounced difference between increasing and decreasing q. The nonlinear trend in TSF is to be expected as the tunnel heats up, with the greatest rates of change at the highest airspeeds. Swashplate temperatures (not shown) showed trends similar to balance ΔT, so the temperature trends are not artifacts of the balance or its transducers.

Comparing Figs. 11 and 12, the *linear* part of the NF trends occurs over the same range of q as the constant part of the ΔT trend. The shape of the static temperature trend (Fig. 13) appears to match that of the hysteresis bands for B3 and B4 (Fig. 11) for q>50 lb/ft^2. These comparisons strongly suggest that the nonlinearities in the NF responses, including hysteresis, are caused by temperature.

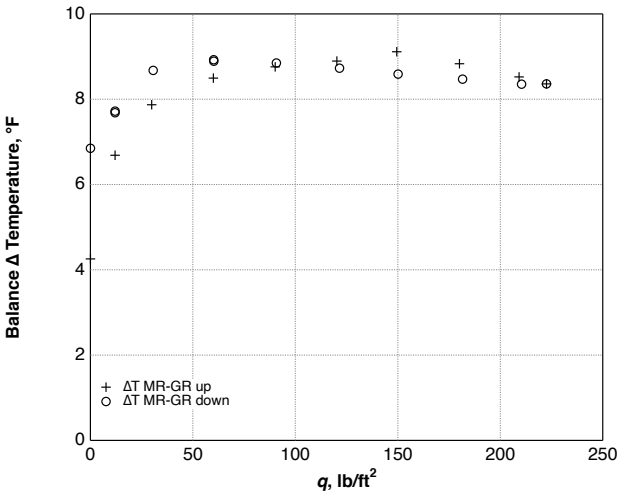

Fig. 12. Balance metric−ground ring average temperatures.

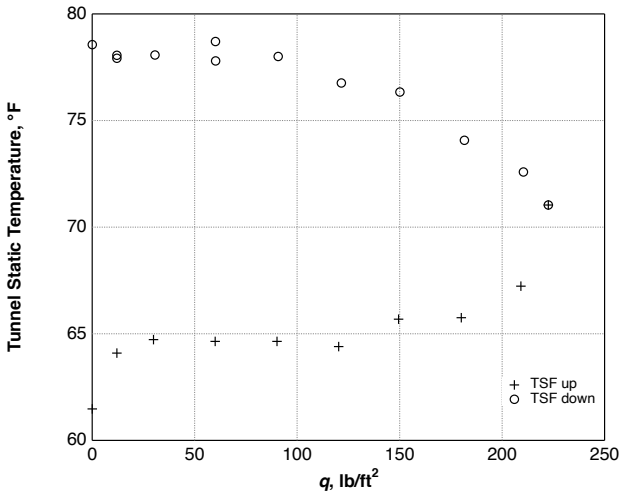

Fig. 13. Tunnel static temperature TSF versus q.

A reasonable assumption is that with the rotor installed and the mast module bearings loaded, the balance metric and ground ring temperatures quickly assume an approximately constant difference. It is therefore appropriate to select tare data over the range of constant ΔT, hence q>50 lb/ft^2 (Fig. 12). Over this range, the NF data show approximately equal slopes for both B3 and B4, and for increasing and decreasing q.

What is required for aerodynamic tares is the linear part of the trend, without hysteresis. A multiple linear regression with terms in q and TSF will determine the linear part. However, the term in TSF must be discarded for data processing because tunnel temperature varies with the weather and time of day. (It is assumed that outside conditions did not appreciably affect tunnel temperature over the duration of the tare data run.) Furthermore, the aerodynamic tare must equal zero at zero airspeed, so the intercept must also be discarded, or at least minimized.

Figure 14 shows curve fits of NF to q and TSF for the B3 and B4 balances separately. Here, the fits were derived from data only above q=50 lb/ft^2. For both balances, including TSF in the fit gave a good match to the hysteresis, more so for B3 than for B4.

The decreasing trend in the B3 data (Figs. 11 and 14), extrapolated to zero q, comes very close to zero load. However, this result is affected by instrumentation initialization (zeros and R-cals) and does not necessarily mean that the decreasing trend is more accurate than any other subset of the data.

Attempts to fit NF to either balance ΔT or to TSF over the full range of airspeed did not yield good results. The nonlinear trends at low q were approximately captured, but not the hysteresis above 50 lb/ft^2. Similar difficulties were seen for fits to swashplate temperature (not shown). Fits to internal spinner pressure gave good fits to hysteresis above 50 lb/ft^2, but not to nonlinear trends at low q. Spinner pressure data are discussed in more detail in Appendix C.

These results do not prove cause and effect between any temperature measurement and NF, because all such data are correlated with time. Temperature is used here as a guide to selecting data appropriate for determining tares.

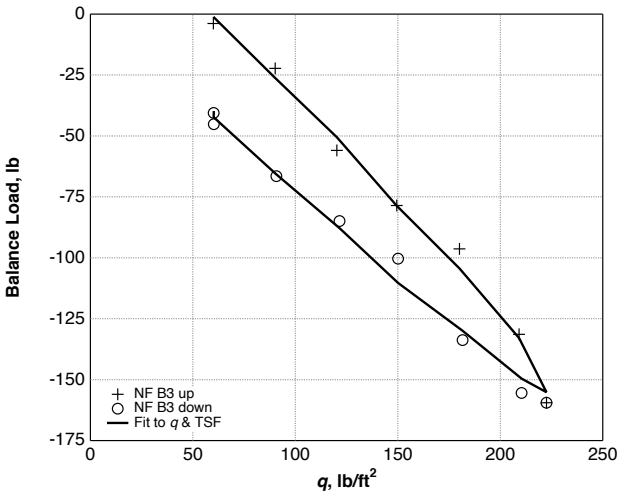

Fig. 14(a). NF B3 fit to q and TSF.

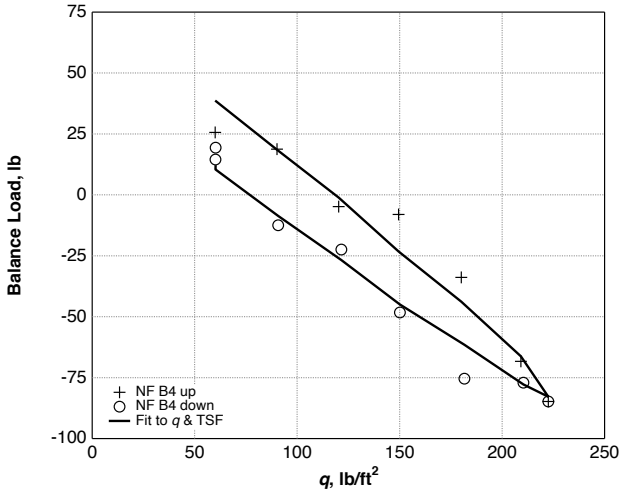

Fig. 14(b). NF B4 fit to q and TSF.

The fit to the B3 data yields an estimate of spinner drag with lower uncertainty than the fit to B4 (se_q=0.026 vs. se_q=0.042). Furthermore, the B3 data have a much smaller zero offset than the B4 data. Therefore, it is recommended that the high-speed NF aerodynamic tares be derived from the B3 data exclusively. The result is

Yaw = 0:
NF tare (lb) = −0.833q

This tare value is considerably larger than that predicted by Bell, but is lower than the measured drag of the smaller XV-15 spinner (Ref. 5, Fig. IV-6).

Spinner aerodynamic tares are not well-defined for Yaw < 30 deg and q > 75 lb/ft^2 (Fig. 10), but that condition is near the limits of the aircraft flight envelope. The simplified version of the tare (0.833 ft^2 flat-plate area) is sufficient.

SF Tares

Figures 5 and 6 show that SF was non-zero and varied with yaw angle. This result can be explained by the Magnus effect from the rotating spinner. It was thought that aerodynamic interference from the rotor blades would minimize the Magnus effect, but a data run with exposed yokes suggested that the Magnus effect remains. See Appendix A for discussion.

The Magnus effect is concentrated over a narrow range of yaw angles. Below 90 deg yaw, the trend closely follows a Gaussian normal distribution (inverted), although this is surely coincidental. A cosine−1 function was also examined, but required scaling yaw angle to non-physical values. See the section Alternative SF Tare Equations in Appendix B for details. Polynomial curve fits gave poor results, although not all possibilities were examined, given the acceptable results with other methods.

Normalizing SF by velocity V (Fig. 15) gave better results than normalizing by q, which is consistent with the Magnus effect. The data do not appear to follow a pure Magnus effect, but the test matrix of yaw and airspeed was too limited to reliably determine any other relationship between SF and V. Normalizing by q gave very different trends at 12 lb/ft^2 vs. the trends at 36 and 75 lb/ft^2 (not shown). Normalizing by V gave imperfect results (Fig. 15), but the resulting data distribution was better suited for finding tare equations useable at all airspeeds.

Seifert (Ref. 6) gives a readable overview of the Magnus effect, and suggests that the lift should depend on both V and V^2. However, the complete equations require multiple inputs not readily derived from wind-tunnel data, and constructing a more accurate model from only three airspeeds and one rotational speed would be problematic. A tare model dependent only on Ψ and V is sufficient here.

A general solution for SF would ideally include a term in rotor speed Ω. No aerodynamic tare data were taken with variable Ω, much less a matrix of Ω vs. V, so the relationship of the Magnus effect to V vs Ω cannot be effectively explored here. However, the Magnus effect is important only at large yaw angles—equivalent to large nacelle angles in flight—which would be encountered only at helicopter mode rotor speed. It is therefore sufficient to define SF tares only for large nacelle angles and helicopter rotor speed.

There were no grounds for preferring B3 or B4, so both sets of data were used. A consequence is that the curve fits closely match neither balance over the full range of yaw angles.

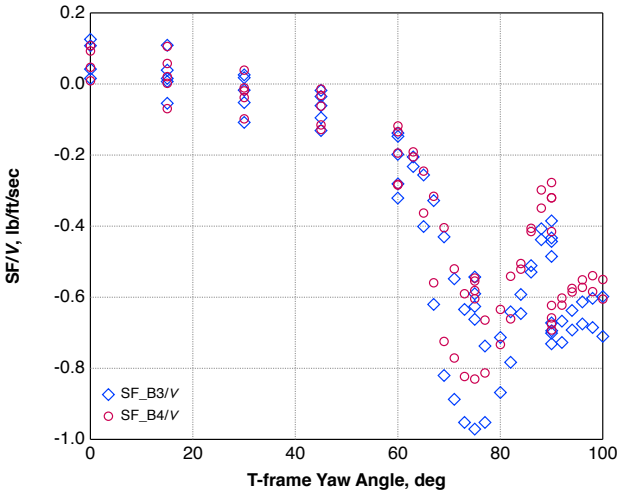

Fig. 15. SF/V tare data at three values of V.

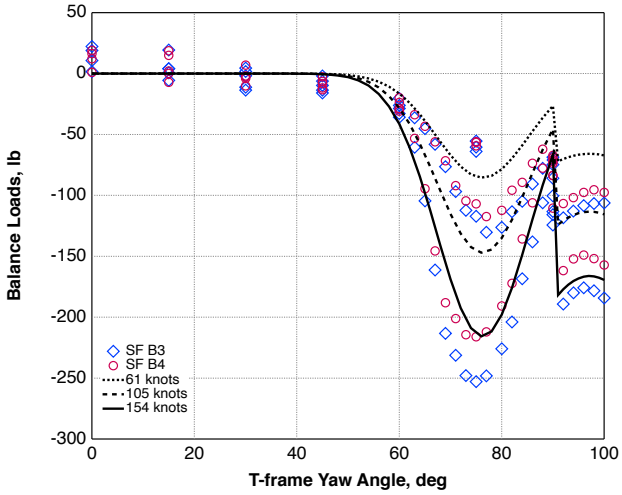

Fig. 16. Aero tare model for SF.

A reasonable fit to the data was achieved by adjusting the input parameters to the normal distribution with the Excel Solver utility. While nonphysical, this method has the two advantages of applying over a wide range of yaw angles (0-90) and requiring only three input parameters. It also gave a decidedly better fit to the data than any polynomial fit up to sixth order. As with AF and NF, the trend above 90 deg yaw was fitted with a second-order polynomial in yaw. The results are shown in Fig. 16 and the coefficients given here:

Yaw < 90, from a least-squares fit to the normal distribution:
SF tare (lb) = $-31.5V*N(\Psi; 76.3, 8.96)$,

where $N(x; \mu, \sigma)$ is the probability density function with normal distribution (Ref. 7);
Mean=76.3 deg, Standard Deviation=8.96 deg, Scale= −31.5

Yaw ≥ 90, from 2nd-order curve fit to SF/V:
SF tare (lb) = $-2.65\text{E}{-}03V\Psi^2 + 0.515V\Psi - 26.1V$

Note that SF depends upon V (knots), not q (lb/ft^2). The velocity units in the curve fits and tare equations for SF are knots, as convenient for data processing. Figure 15 uses velocity units of ft/sec for plotting.

There is a slight negative slope of SF/V vs. yaw angle below 60 deg, but the variation is barely greater than the $\pm 2\sigma$ uncertainty. Furthermore, SF should be zero at zero yaw. The slope at low yaw angle is therefore ignored here.

Strictly speaking, the tare is undefined at 90 deg yaw. Tares at 90 deg are assigned to the high-angle equation because the trends in Fig. 15 appear to favor that interpretation.

PM Tares

PM/q trends (Fig. 17) closely resembled AF/q (Fig. 7), so the curve fits follow the same pattern:

Yaw ≤ 90, from 3rd-order curve fit to PM/q:
PM tare (lb) = $-1.66\text{E}{-}04q\Psi^3 + 6.75\text{E}{-}03q\Psi^2 + 1.31q\Psi + 0.00q$

Yaw > 90, from 2nd-order curve fit to PM/q:
PM tare (lb) = $6.00\text{E}{-}02q\Psi^2 - 13.0q\Psi + 719q$

The term in q for Yaw ≤ 90 was forced to zero to prevent excessive values at low Ψ and high q (airplane mode). If the fit includes a non-zero term in q, the differences are $<2\pm\sigma$ (balance uncertainty) everywhere but Ψ≈0 (barely visible at the scale of Fig. 18).

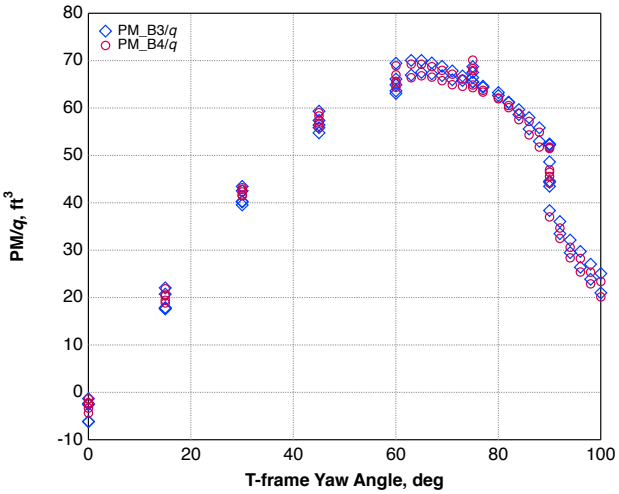

Fig. 17. PM/q tare data at three values of q.

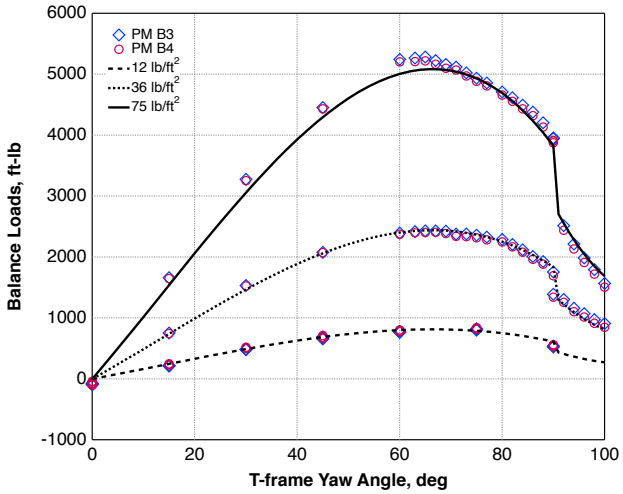

Fig. 18. Aero tare model for PM.

RM Tares

RM/V trends (Fig. 19) closely resembled SF/V (Fig. 15), so the curve fits follow the same pattern:

Yaw < 90, from a least-squares fit to the normal distribution:
RM tare (lb)= $-277V*N(\Psi; 76.1, 9.99)$,

where $N(x; \mu, \sigma)$ is the probability density function with normal distribution (Ref. 7);
Mean=76.1 deg, Standard Deviation=9.99 deg, Scale= −277

Yaw ≥ 90, from 2nd-order curve fit to RM/V:
RM tare (lb) = $-1.71\text{E}{-}02V\Psi^2 + 3.36V\Psi - 175V$

The results are shown in Fig. 20.

Note that RM depends upon V (knots), not q (lb/ft^2). The velocity units in the curve fits and tare equations for RM are knots, as convenient for data processing. Figure 19 uses velocity units of ft/sec for plotting.

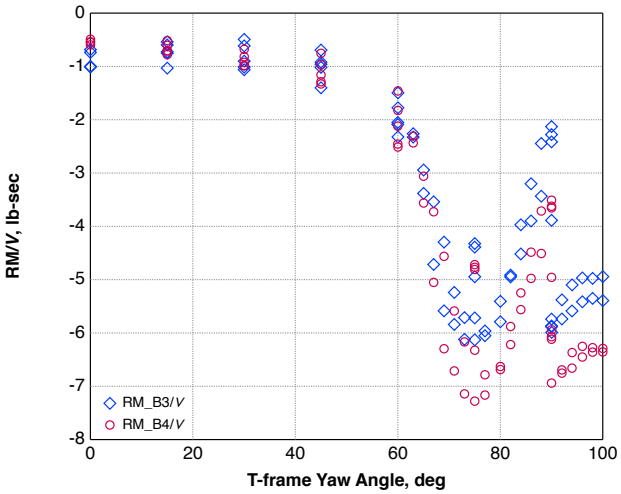

Fig. 19. RM/V tare data at three values of V.

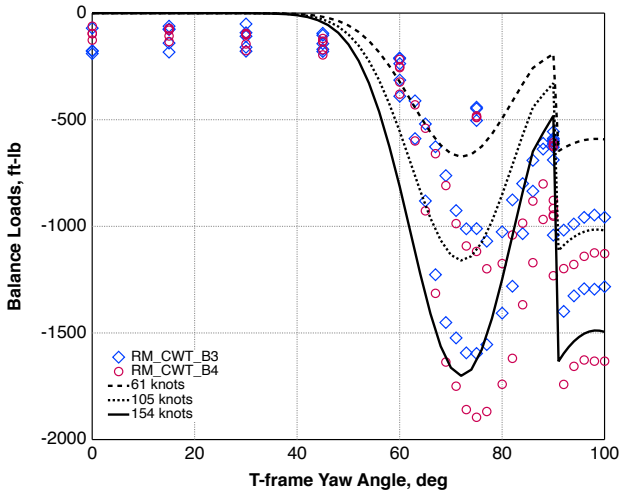

Fig. 20. Aero tare model for RM.

YM Tares

Ideally, there should be zero effect of airspeed and yaw angle on YM tares. The data shown in Fig. 6 are consistent with this assumption (all data are within 0.7% of the calibrated torque range). Therefore, no tare corrections are needed for YM.

ROTOR SHAFT STRAIN-GAGE TARES

The rotor shaft has strain gages mounted at multiple locations near the rotor hub; the gages are intended primarily for loads monitoring. Non-rotating hub loads can be derived from any two pairs of orthogonal gages located at different locations along the shaft. These derived loads include only in-plane forces and moments; axial (thrust) and torque loads are sensed only as interactions. Although inherently less accurate than the balance, the shaft gage sensitivities and ranges more closely match the actual 699 rotor loads. Forces and moments derived from the shaft gages are therefore useful, provided researchers keep in mind their limitations. The shaft loads require tare corrections similar but not identical to the rotor balance measurements.

For the strain gages in question, the term “mast” is technically more accurate, but the term “shaft” is used by convention for wind-tunnel data processing. The latter term is used here to facilitate cross-references to the test database, which uses the “_SH_” tag to distinguish shaft loads from rotor balance loads. All shaft loads are measured in the hub-centered “BD” axis system.

The shaft-load measurements are derived from two sets of strain gage pairs, designated “A” and “B”. The A loads use the strain gage pairs furthest apart; the B loads use the pairs closer together. The B load measurements are in principle less accurate than the A loads because the moment arm is shorter, hence more sensitive to any dimensional error. However, the B values do not include loads from the swashplate linkage or counterweight, and are therefore more representative of pure rotor loads. Furthermore, the strain gages used for the A and B loads are different distances from the spinner supports, and therefore react differently to spinner loads. Hence, the A and B shaft load measurements require different spinner tare corrections.

The shaft strain gages received only a simple bench calibration with far fewer data points than the rotor balance calibration. The calibration data do not permit exact comparisons with the uncertainties given in Table 2, so the plots given below do not include error bars.

Weight Tares for Curve Fits

Weight tares are required with the shaft rotating to get correct averages. Weight tares were extracted from the same runs as the aerodynamic data, during which four data points were taken at full shaft rpm and zero airspeed. The number of data points is very small, but include data at both 0 and 90 deg yaw angles (two zeros at each angle), and the data are consistent. Table 3 lists the weight tares and statistics. The standard deviations are very small compared to full-scale rotor loads, so no further analysis was attempted.

The average weight tares were subtracted from the data before aerodynamic tares were derived. Note that these weight tares apply only to the spinner on, rotor off configuration and are meant to be used only for computing aerodynamic tares. It is assumed that for rotor-on data, equivalent rotor weight tares will be subtracted before the aerodynamic tares are applied.

Table 3. Shaft strain gage weight tares (rotor off).

Statistics (lb)	AF_BD_SH_A	AF_BD_SH_B	SF_BD_SH_A	SF_BD_SH_B
Average	0.6342	-2.2954	165.7998	60.0201
Min	0.4366	-2.3701	165.5160	58.6242
Max	0.8073	-2.1395	166.1070	61.6068
Std. dev.	0.1588	0.1072	0.3211	1.2237

Statistics (ft-lb)	PM_BD_SH_A	PM_BD_SH_B	RM_BD_SH_A	RM_BD_SH_B
Average	-1.0759	-0.0886	37.6428	73.2905
Min	-1.3720	-0.3744	37.4670	72.6414
Max	-0.7853	0.2078	37.9179	73.6598
Std. dev.	0.2957	0.2778	0.1944	0.4490

Shaft Aerodynamic Tares

Ideally, the rotor balance and shaft aerodynamic tares would be identical, but the shaft gages respond differently to test conditions than does the balance. Therefore, aerodynamic tares were developed separately for shaft loads.

Figure 21 shows the data used for the shaft gage aerodynamic tare analyses, here for both the A and B gage sets with weight tares subtracted. The trends are generally similar to those of Fig. 6, although the magnitudes of the A- and B-set responses are clearly different. The magnitudes of the moment tares (PM and RM) are much reduced from those in Fig. 6 because they are in a different axis system (balance center vs. hub).

For AF and SF loads, the shaft A-gage data match the balance data better than the B-gage data (compare Figs. 6 and 21). The PM and RM loads are in different axis systems, which makes direct comparison problematic. It is recommended that only the A-gage data be used for shaft weight and aero tares, but B-gage data are analyzed here for completeness.

Construction of a tare model for the shaft gages employed the same methods as for the balance measurements. Little effort was made to customize the curve fits for the shaft data: in all cases, the same regression routines were applied to the same test conditions as for the balance tares, but with shaft-gage data replacing the balance data. A few points at 90 deg yaw were deleted to get good fits at that angle. More accurate tare models should certainly be possible, but are difficult to justify without more comprehensive strain-gage calibrations to define the limiting measurement accuracy.

All shaft tares should equal zero at q=0 lb/ft^2 and at Ψ=0 deg. Subtraction of weight tares largely achieved such, and the curve fits were forced to equal zero load at zero airspeed and yaw. All shaft tare data were taken at helicopter-mode tip speed (569 rpm). As with the balance tares, shaft tares are defined only in the range $0 \le \Psi \le 110$ deg.

The curve-fit procedures closely follow those used for the balance tares, so only summary results are presented here without discussion. Results for A and B strain gages are presented separately in Figs. 22-29. In the following figures, individual points are weight-corrected data at actual yaw angles, and lines are predictions by the tare equations at arbitrary yaw angles. Vertical scales are freely adjusted to match the data.

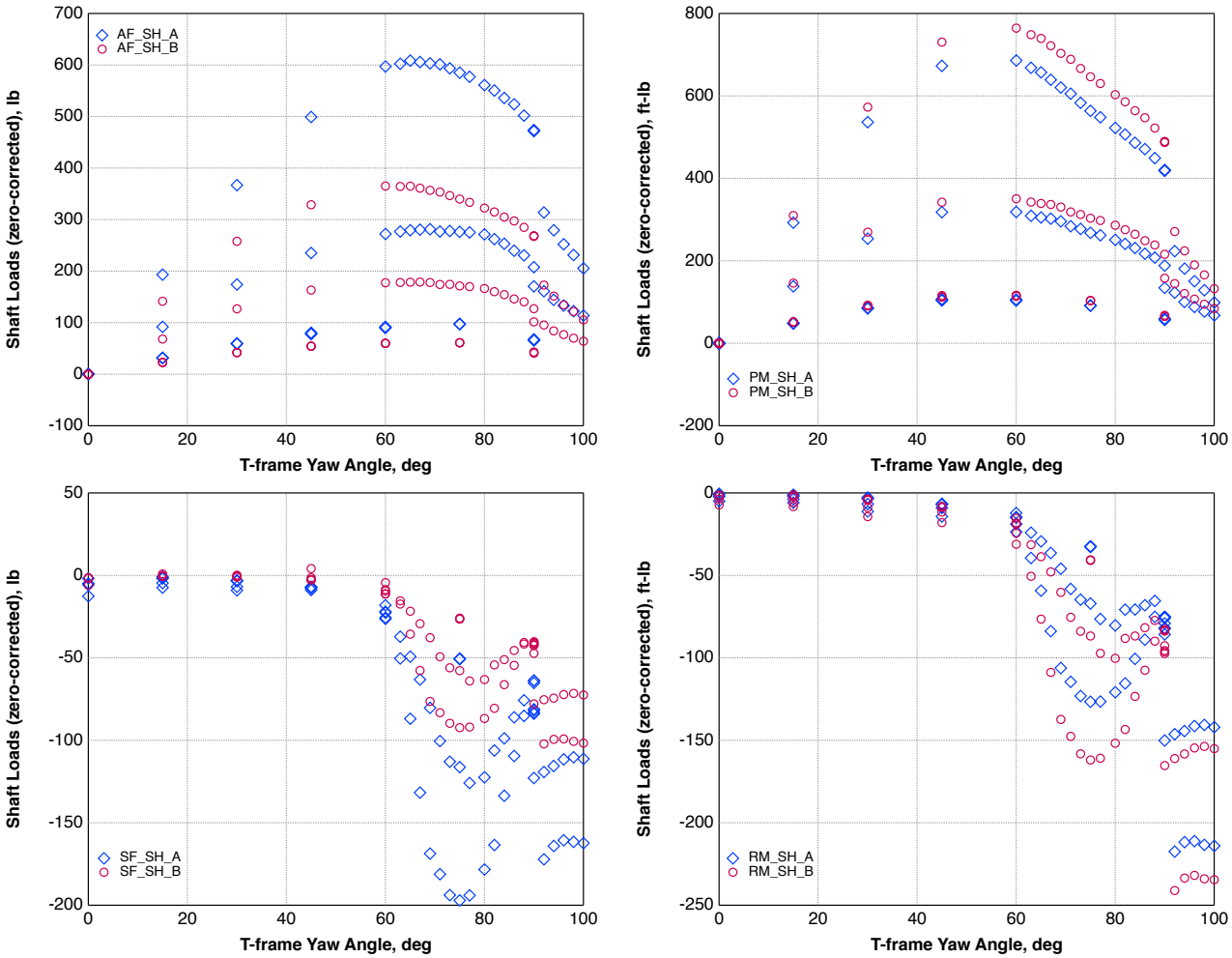

Fig. 21. Rotor shaft strain-gage tare variations with yaw angle, at fine increments; q=12, 36, and 75 lb/ft2.

AF Shaft Tares

Yaw ≤ 90:

$AF\ (A)\ tare\ (lb) = -1.44E{-}05q\Psi^3 + 2.15E{-}03q\Psi^2 + 0.168q\Psi$

Yaw > 90:

$AF\ (A)\ tare\ (lb) = 6.62E{-}03q\Psi^2 - 1.44q\Psi + 80.7q$

Yaw ≤ 90:

$AF\ (B)\ tare\ (lb) = -5.12E{-}06q\Psi^3 - 6.20E{-}04q\Psi^2 + 0.138q\Psi$

Yaw > 90:

$AF\ (B)\ tare\ (lb) = 4.40E{-}03q\Psi^2 - 0.953q\Psi + 52.9q$

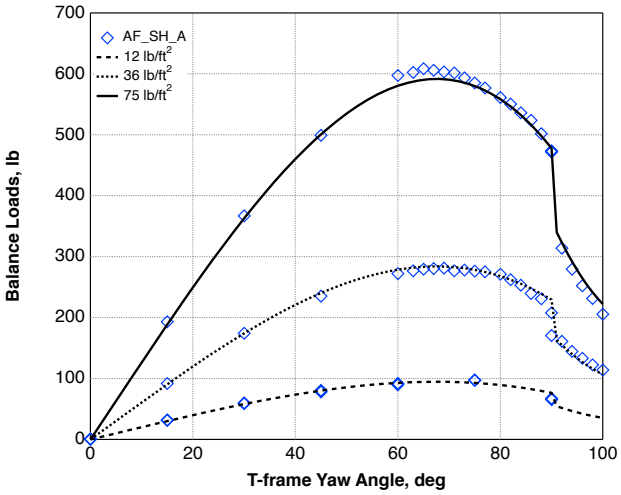

Fig. 22. Aero tare model for AF_SH_A.

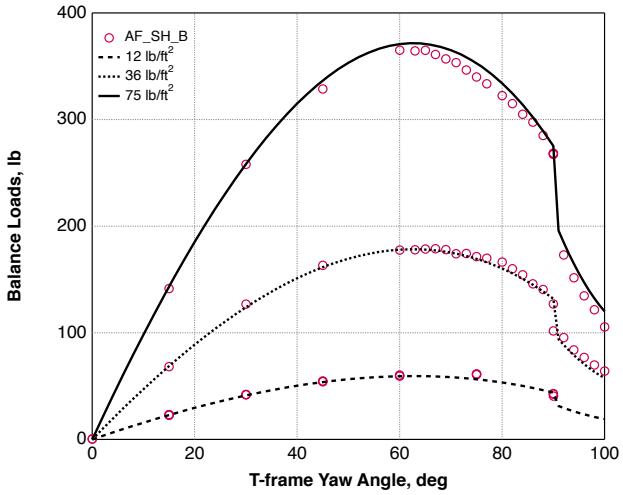

Fig. 23. Aero tare model for AF_SH_B.

SF Shaft Tares

Yaw < 90:

$SF\ (A)\ tare\ (lb) = -28.9V^{*}N(\Psi;\ 76.5,9.23),$

where $N(x;\ \mu,\ \sigma)$ is the probability density function with normal distribution;
Mean=76.5 deg, Standard Deviation=9.23 deg, Scale= −28.9

Yaw ≥ 90:

$SF\ (A)\ tare\ (lb) = -2.25E{-}03V\Psi^2 + 0.441V\Psi - 22.6V$

Yaw < 90:

$SF\ (B)\ tare\ (lb) = -13.6V^{*}N(\Psi;\ 77.1,8.93),$

Yaw ≥ 90:

$SF\ (B)\ tare\ (lb) = -9.60E{-}04V\Psi^2 + 0.186V\Psi - 9.70V$

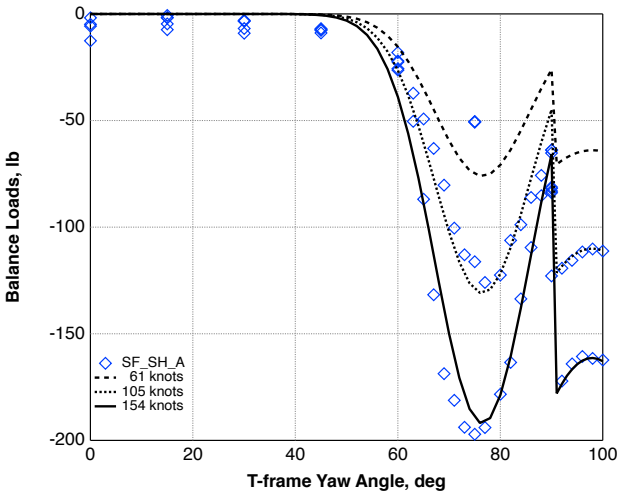

Fig. 24. Aero tare model for SF_SH_A.

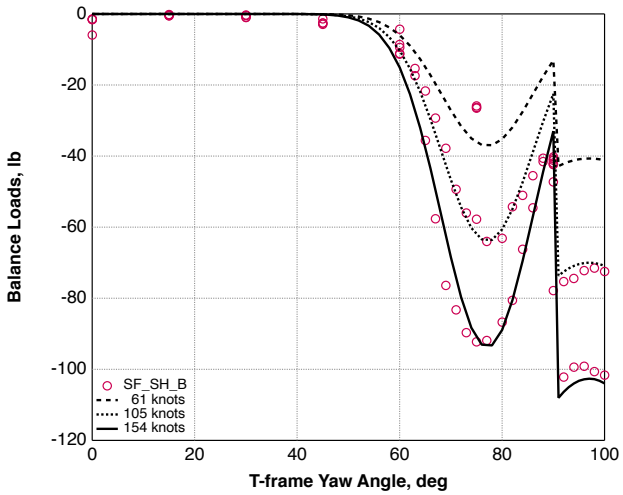

Fig. 25. Aero tare model for SF_SH_B.

PM Shaft Tares

Yaw ≤ 90:

$PM\ (A)\ tare\ (lb) = 2.44E{-}07q\Psi^3 - 2.98E{-}03q\Psi^2 + 0.324q\Psi$

Yaw > 90:

$PM\ (A)\ tare\ (lb) = 1.04E{-}02q\Psi^2 - 2.18q\Psi + 116q$

In principle, the cubic term in the first equation (2.44E-07) could be set =0 with negligible effect on accuracy. It has been left in this form to match the coding for the rotor balance PM aero tare.

Yaw ≤ 90:

$PM\ (B)\ tare\ (lb) = -2.87E{-}06q\Psi^3 - 2.70E{-}03q\Psi^2 + 0.334q\Psi$

Yaw > 90:

$PM\ (B)\ tare\ (lb) = 1.11E{-}02q\Psi^2 - 2.34q\Psi + 125q$

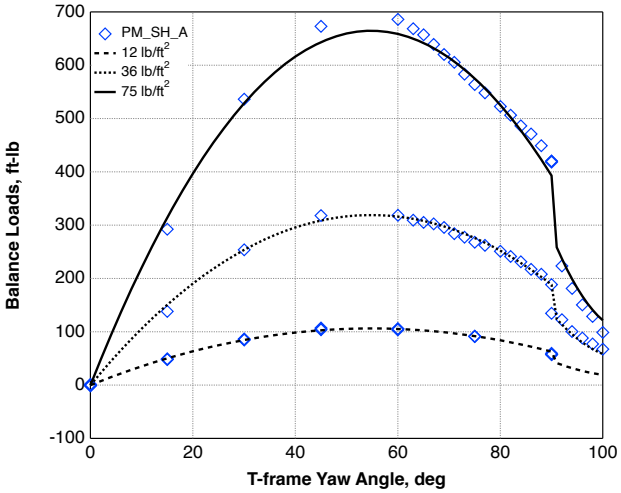

Fig. 26. Aero tare model for PM_SH_A.

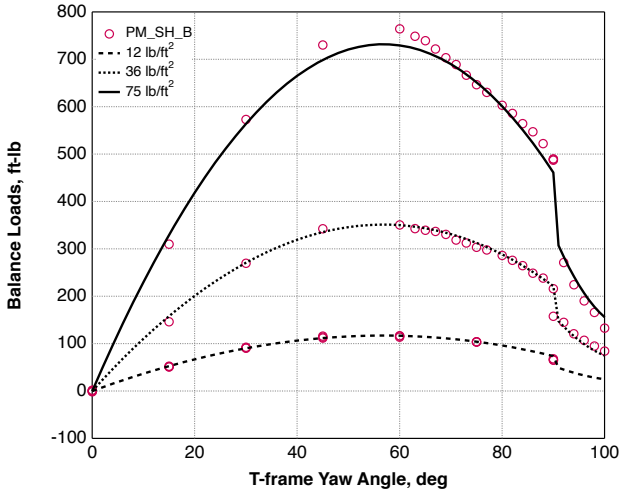

Fig. 27. Aero tare model for PM_SH_B.

RM Shaft Tares

Yaw < 90:
RM (A) tare (lb) = −21.1*V***N*(Ψ; 77.9,10.64),

where $N(x; \mu, \sigma)$ is the probability density function with normal distribution;
Mean=77.9 deg, Standard Deviation=10.64 deg, Scale= −21.1

Yaw ≥ 90:
RM (A) tare (lb) = −1.61E−03$V\Psi^2$ + 0.312$V\Psi$ – 16.5V

Yaw < 90:
RM (B) tare (lb) = −26.2V**N*(Ψ; 77.4,10.39),

Yaw ≥ 90:
RM (B) tare (lb) = −2.04E−03$V\Psi^2$ + 0.398$V\Psi$ – 20.9V

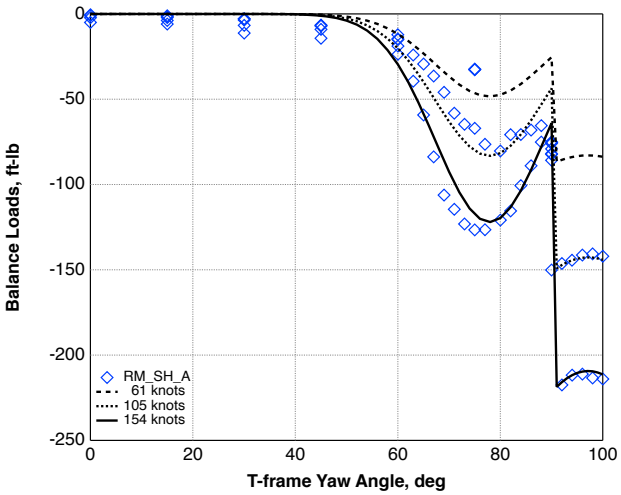

Fig. 28. Aero tare model for RM_SH_A.

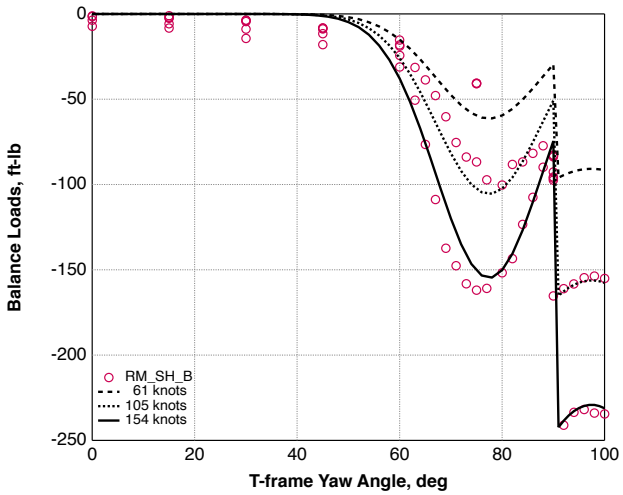

Fig. 29. Aero tare model for RM_SH_B.

Limitations of the Shaft Tare Model

Although aerodynamic tare equations are provided for both the A and B shaft gages, it is recommended to use only the A gages and associated tares. The shaft A loads match the balance loads much better than the B loads; compare AF and SF in Figs. 6 and 21 (the moments PM and RM should not match because of the offset between the hub and balance moment centers). With the rotor installed, the discrepancy between the A and B shaft loads is negligible, but the rotor loads are much greater than the spinner aerodynamic loads and have a different load distribution than the spinner supports. Finally, the shaft A loads should be more accurate than the B loads, for reasons mentioned earlier. None of these observations actually prove that the shaft B loads are incorrect. A comprehensive calibration of the rotor shaft strain gages, with the shaft installed on the TTR and full rotor weight pre-load, may provide some insight into the different responses of the two gage set.

RECOMMENDATIONS

The tare data at minimum airspeed (nominally 60 knots, or q=12 lb/ft^2) were more erratic than at higher airspeeds, indicating that 60 knots was too slow to fully stabilize the flow in all cases. Fewer than eight airspeeds would perhaps be sufficient to map out the overall behavior at coarse yaw increments (Fig. 5), but at least four airspeeds are recommended at fine yaw increments (Fig. 6). If maximum dynamic pressure is 75 lb/ft^2, then steps of 20 lb/ft^2 may be sufficient: 15, 35, 55, and 75 lb/ft^2.

The tare data collected during this entry did not include any non-zero yaw angles at very high speed (>155 knots), nor did it include yaw variations at fine increments near zero yaw at any speed. If future test objectives include simulation of maneuvers at high speed, then fine yaw variations over a limited range (perhaps 0-10 deg) are recommended at a few high-speed conditions.

The transition from axial flow (net spinner drag) to conversion mode (net spinner lift) is poorly defined. Should accurate performance and trim measurements be required at low yaw (nacelle) angles, then finer yaw variations may be needed near 30 deg.

The bench calibration of the rotor shaft strain gages was limited in scope. Those gages should be recalibrated when installed on the TTR, at a variety of azimuth angles and with and without a rotor weight preload.

APPENDIX A: LOADS WITH EXPOSED YOKE

A single tare run was performed with the blades removed. The hub, including yoke and outboard bearings, was left installed. The yoke arms were covered with protective wrapping and tape (Fig. A1). The results are plotted in Fig. A2.

Fig. A1. Yoke and spinner configuration for tare checks.

The ideal test would have included aerodynamic interactions between the spinner and blade roots, but without any blade lifting surfaces. Unfortunately, such a test is not possible. The blade roots are large enough to completely enclose the yoke arms and bearings, such that the outboard bearings are inside the blade airfoil sections. It is therefore impossible to take aerodynamic tares with the hub installed but without any blade lifting surfaces. The yoke tares were a practical compromise and were incomplete in any case; they cannot be used to identify true spinner tares.

Despite these limitations, useful conclusions can be drawn from the data. Comparing the plots below with Fig. 6, nearly all loads were of similar magnitude and had similar trends. YM had much larger magnitudes with the yoke exposed, but this was to be expected.

The magnitudes of SF and RM were reduced compared with the bare spinner, but the Magnus effect was still very evident. The conclusion is that the blades will not destroy the Magnus effect, so the SF and RM aero tares should not be set to zero.

Somewhat disturbingly, inconsistencies between the B3 and B4 balances remain for SF and RM: B3 shows a stronger response than B4 for SF, but a weaker response for RM. The conclusion is that the discrepancy is a feature of the balance and not an artifact of the test conditions. The differences are rarely greater than the $\pm 2\sigma$ calibration uncertainty, but the discrepancies are consistent and grow worse with increasing yaw angle.

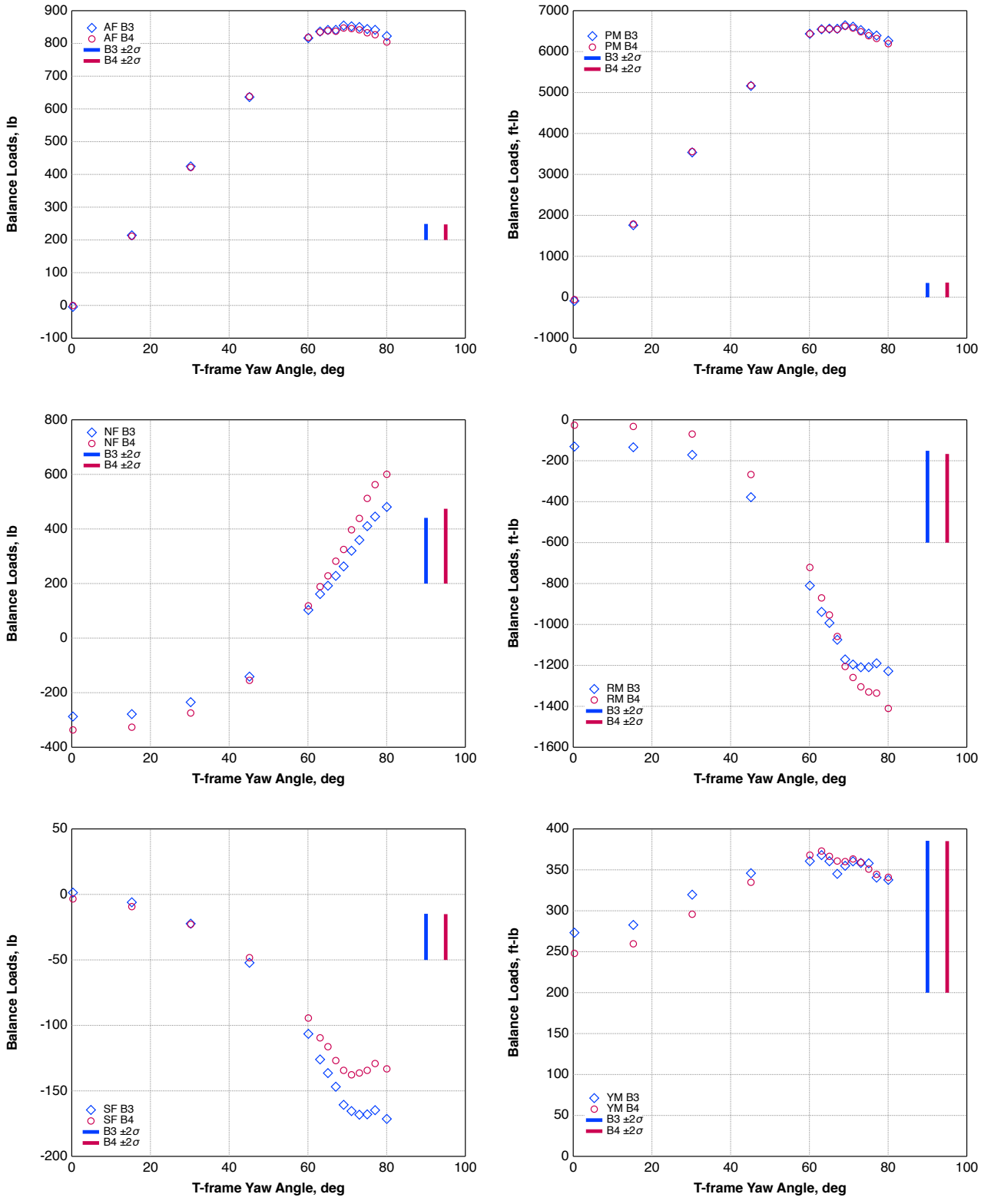

Fig. A2. Aerodynamic tare variations with yaw angle, yoke installed.

APPENDIX B: CURVE-FIT PARAMETERS

For the aerodynamic tare curve fits, the dependent variable was sometimes the measured load, and sometimes the normalized load (e.g. AF/q). The standard errors should be interpreted accordingly. For SF and RM (normalized as SF/V and RM/V), the Excel Solver was used to minimize the squared error between measured and predicted load. The standard error of estimate was then estimated from the summed squared error, taking the degrees of freedom to be one less than the number of data points, minus the number of parameters optimized.

For the record, all yaw-sweep aerodynamic tare data used for curve fits were acquired during runs 28, 31 and 33. All high-speed tare data were acquired during run 14.

Balance Tare Parameters

AF/q 3rd-order fit, $\Psi < 90$

	Ψ^3	Ψ^2	Ψ	b
Mn	-2.264E-05	1.405E-03	0.1402	-0.1004
SEb	1.982E-06	2.679E-04	0.0100	0.09700
r2, SEy	0.9888	0.3187		
F, df	3070.3	104		
SSreg, SSresid	935.27	10.56		

AF/q 2nd-order fit, $\Psi > 90$

	Ψ^2	Ψ	b
Mn	0.00849	-1.806	99.31
SEb	0.01459	2.801	134.37
r2, SEy	0.6106	0.4355	
F, df	13.326	17	
SSreg, SSresid	5.055	3.224	

NF fit to TSF and q, $\Psi = 0$

	TSF	q	b
Mn	-2.923	-0.8327	237.81
SEb	0.2710	0.02633	20.38
r2, SEy	0.9893	5.453	
F, df	510.8	11	
SSreg, SSresid	30375	327.1	

NF 3rd-order fit, $0 < \Psi < 90$

	$q\Psi^3$	$q\Psi^2$	$q\Psi$	b
Mn	2.212E-05	0.003795	-0.09467	-10.41
SEb	2.907E-06	0.004157	0.01519	4.211
r2, SEy	0.9859	19.18		
F, df	1355	58		
SSreg, SSresid	1494655	21331		

NF 2nd-order fit, $\Psi > 90$

	$q\Psi^2$	$q\Psi$	b
Mn	-0.0008637	0.1079	27.71
SEb	0.0001529	0.01486	7.350
r2, SEy	0.9821	7.686	
F, df	191.91	7	
SSreg, SSresid	22675	413.5	

SF fit, $\Psi < 90$, normal distribution

Mean	76.27
Std Dev	8.958
Scale	-31.45
No. samples	108
≈Std. error	19.25

SF/*V* 2nd-order fit, $\Psi > 90$

	Ψ^2	Ψ	b
Mn	-0.002645	0.5153	-26.11
SEb	0.001604	0.3042	14.41
r2, SEy	0.3356	0.0828	
F, df	5.8098	23	
SSreg, SSresid	0.07957	0.1575	

Alternative SF fit to $(\cos(\Psi - \Psi_0)) - 1$; $\Psi < 90$

Ψ_0	54.61
Ψ scale	8.332
Magnitude	0.6897
No. samples	68
≈Std. error	23.51

PM/*q* 3rd-order fit, Ψ < 90

	Ψ^3	Ψ^2	Ψ	b
Mn	-1.382E-04	2.107E-03	1.5364	-3.1807
SEb	9.870E-06	1.334E-03	0.04991	0.4831
r2, SEy	0.9951	1.5869		
F, df	7085.9	104		
SSreg, SSresid	53529	261.89		

PM/*q* 2nd-order fit, Ψ > 90

	Ψ^2	Ψ	b
Mn	0.06004	-12.973	719.42
SEb	0.05837	11.208	537.63
r2, SEy	0.8673	1.7425	
F, df	55.560	17	
SSreg, SSresid	337.38	51.615	

RM/*V* fit, Ψ < 90, normal distribution

Mean	76.213
Std Dev	9.989
Scale	-276.55
No. samples	108
≈Std. error	132.89

RM/*V* 2nd-order fit, Ψ > 90

	Ψ^2	Ψ	b
Mn	-0.01706	3.3587	-174.94
SEb	0.03696	7.0969	340.43
r2, SEy	0.0613	1.1033	
F, df	0.5549	17	
SSreg, SSresid	1.3510	20.695	

Shaft Tare Parameters

AF_SH_A/*q* 3rd-order fit, Ψ < 90 (b is forced to equal 0)

	Ψ^3	Ψ^2	Ψ	b
Mn	-1.437E-05	2.150E-04	0.16783	0.00
SEb	1.215E-06	1.546E-04	0.00485	
r2, SEy	0.9995	0.1531		
F, df	33112.81	51		
SSreg, SSresid	2329.49	1.20		

AF_SH_A/*q* 2nd-order fit, Ψ > 90

	Ψ^2	Ψ	b
Mn	0.00662	-1.439	80.66
SEb	0.00933	1.791	85.93
r2, SEy	0.8931	0.1969	
F, df	29.253	7	
SSreg, SSresid	2.269	0.271	

AF_SH_B/*q* 3rd-order fit, Ψ < 90 (b is forced to equal 0)

	Ψ^3	Ψ^2	Ψ	b
Mn	-5.119E-06	-6.198E-04	0.13802	0.00
SEb	1.003E-06	1.276E-04	0.00400	
r2, SEy	0.9991	0.1264		
F, df	19099.38	51		
SSreg, SSresid	915.46	0.81		

AF_SH_B/*q* 2nd-order fit, Ψ > 90

	Ψ^2	Ψ	b
Mn	0.00440	-0.953	52.87
SEb	0.00952	1.828	87.68
r2, SEy	0.7689	0.2009	
F, df	11.643	7	
SSreg, SSresid	0.940	0.283	

SF_SH_A fit, Ψ < 90, normal distribution

Mean	76.49
Std Dev	9.23
Scale	-28.86
No. samples	54
≈Std. error	11.13

SF_SH_A/*V* 2nd-order fit, Ψ > 90

	Ψ^2	Ψ	b
Mn	-0.002253	0.4412	-22.65
SEb	0.000605	0.1161	5.57
r2, SEy	0.8779	0.0128	
F, df	25.1716	7	
SSreg, SSresid	0.00820	0.0011	

SF_SH_B fit, $\Psi < 90$, normal distribution

Mean	77.08
Std Dev	8.93
Scale	-13.63
No. samples	54
≈Std. error	5.10

SF_SH_B/*V* 2nd-order fit, $\Psi > 90$

	Ψ^2	Ψ	b
Mn	-0.000960	0.1862	-9.70
SEb	0.001320	0.2536	12.16
r2, SEy	0.1165	0.0279	
F, df	0.4617	7	
SSreg, SSresid	0.00072	0.0054	

PM_SH_A/*q* 3rd-order fit, $\Psi < 90$ (b is forced to equal 0)

	Ψ^3	Ψ^2	Ψ	b
Mn	2.439E-07	-2.976E-03	0.32412	0.00
SEb	1.290E-06	1.641E-04	0.00515	
r2, SEy	0.9995	0.1626		
F, df	34427.17	51		
SSreg, SSresid	2730.98	1.35		

PM_SH_A/*q* 2nd-order fit, $\Psi > 90$

	Ψ^2	Ψ	b
Mn	0.01035	-2.180	116.10
SEb	0.01274	2.446	117.32
r2, SEy	0.8562	0.2689	
F, df	20.846	7	
SSreg, SSresid	3.014	0.506	

PM_SH_B/*q* 3rd-order fit, $\Psi < 90$ (b is forced to equal 0)

	Ψ^3	Ψ^2	Ψ	b
Mn	-2.872E-06	-2.695E-03	0.33416	0.00
SEb	1.431E-06	1.821E-04	0.00571	
r2, SEy	0.9995	0.1804		
F, df	34692.91	51		
SSreg, SSresid	3388.58	1.66		

PM_SH_B/*q* 3rd-order fit, Ψ < 90 (b is forced to equal 0)

	Ψ^2	Ψ	b
Mn	0.01110	-2.344	125.47
SEb	0.01269	2.437	116.90
r2, SEy	0.8797	0.2679	
F, df	25.595	7	
SSreg, SSresid	3.674	0.502	

RM_SH_A fit, Ψ < 90, normal distribution

Mean	77.91
Std Dev	10.64
Scale	-21.12
No. samples	54
≈Std. error	8.35

RM_SH_A/*V* 2nd-order fit, Ψ > 90

	Ψ^2	Ψ	b
Mn	-0.001606	0.3121	-16.52
SEb	0.000836	0.1606	7.70
r2, SEy	0.5052	0.0177	
F, df	3.5740	7	
SSreg, SSresid	0.00223	0.0022	

RM_SH_B fit, Ψ < 90, normal distribution

Mean	77.43
Std Dev	10.39
Scale	-26.18
No. samples	54
≈Std. error	10.63

RM_SH_B/*V* 2nd-order fit, Ψ > 90

	Ψ^2	Ψ	b
Mn	-0.002042	0.3980	-20.88
SEb	0.001063	0.2041	9.79
r2, SEy	0.5693	0.0224	
F, df	4.6265	7	
SSreg, SSresid	0.00466	0.0035	

APPENDIX C: SPINNER PRESSURE

The difference between tunnel static pressure and internal spinner pressure creates a force on the spinner. On the TTR, this pressure force adds to the thrust load measured by the rotor balance. In practice, the spinner pressure force is negative, so the thrust measured by the balance is reduced by the pressure force. The net effect on an actual aircraft may be different, depending on the construction of the nacelle immediately behind the rotor. The following discussion applies only to the TTR.

TTR has a pressure transducer mounted inside the spinner to measure the internal spinner pressure. There is no spinner backplate or other pressure seal between the rotating spinner, fixed cowling, or rotor balance. The force on the spinner due to internal pressure is calculated as

Spinner Pressure Force = (Hub Pressure − Tunnel Static Pressure) * Spinner Base Area

There is in theory an equal force applied to the non-rotating components immediately behind the spinner. The balance is vented, so any pressure forces on both faces of the metric side of the balance should cancel. If the remaining pressure force on the non-rotating components is the same with and without the rotor installed, then the spinner tare measurements developed in the main body of this report will adequately represent the total tare forces to be subtracted from the balance measurements to get the true rotor forces.

For the TTR airplane-mode data points, thrust was varied while airspeed was held constant. Ideally, the test would have included airspeed sweeps at constant collective and constant thrust. However, holding collective constant would have caused excessive loads, and maintaining constant thrust would have required extended test time at high speed. For the data available, hub pressure varies with thrust at each test airspeed.

The spinner pressure force is plotted in Fig. C1 for the spinner tare data (Run 14) and all wind-on performance data in airplane mode (0-deg yaw) and M_{tip}=0.583 (Runs 75-77, 80-81, and 104). This value of tip speed matches the shaft speed at which rotor-off tare data were taken (478 rpm). Rotor thrust was varied at each airspeed, reaching a maximum value of 6746 lb for M_{tip}=0.583. The rotor-off data have different markers for increasing and decreasing q. The data shown include only thrust sweeps; control excursion data were also taken but are not shown.

Figure C2 plots equivalent data at helicopter-mode tip speed (M_{tip}=0.684, 569 rpm). There are no rotor-off data at 569 rpm, so the 478-rpm data are repeated in Fig. C2. Maximum airspeed for helicopter-mode tip speed was limited to 212 knots (q=144 lb/ft^2), so the horizontal scale is truncated in Fig. C2.

It is evident that spinner pressure decreases with dynamic pressure with the rotor installed, but varies little with the rotor off. The effect is more pronounced at low tip speed (Fig. C1). However, the data show severe scatter and hysteresis. In particular, the data just below q=50 lb/ft^2 (≈120 knots) fall into two groups, each for a different run. The lower group is for Run 76, which is known to have had temperature-control problems. Eliminating the Run 76 data would still leave an inconsistent trend, particularly at low airspeed.

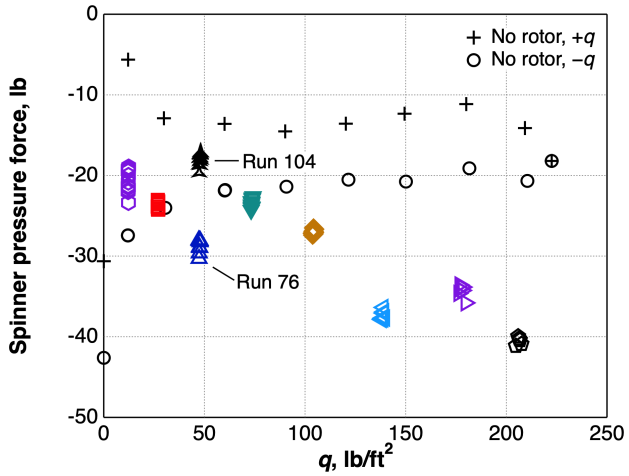

Fig. C1. Spinner pressure force vs dynamic pressure at 478 rpm, M_{tip} = 0.583.

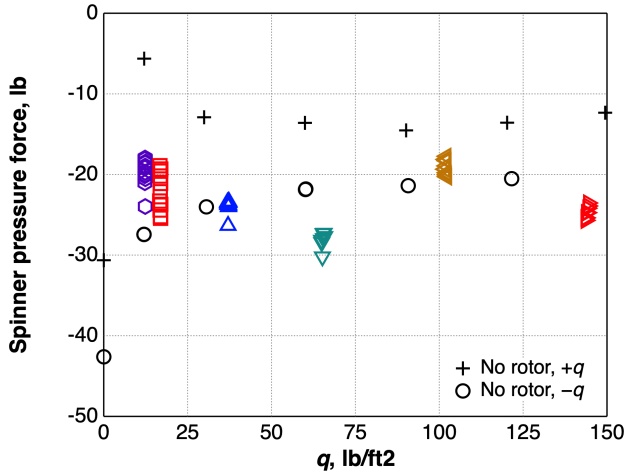

Fig. C2. Spinner pressure force vs dynamic pressure at 569 rpm, M_{tip} = 0.684.

No temperature-control problems are known to apply to the high tip-speed data (Fig. C2), but the trend of spinner pressure force with airspeed is still poorly defined. In both Fig. C1 and C2, there appears to be a linear trend of spinner force with q, broken by offsets between low- and high-speed runs. The scatter at a given airspeed can be attributed to thrust variations, but not the inconsistent linear trends.

The poor trends with airspeed led to further investigations of the behavior of the pressure measurements. NFAC practice is to take nonrotating, zero-airspeed reference data at the beginning and end of each run ("static" data points). The difference between the starting and ending static data is a measure of instrumentation drift. At the static points, the TTR hub pressure should ideally match barometric pressure as measured by the standard NFAC instrumentation.

For all airplane-mode runs, including the rotor-off spinner tare run, the hub pressure drift was greater than the barometric pressure drift or of reversed sign. This discrepancy is a strong indicator that the hub pressure transducer had inadequate temperature compensation. In terms of spinner pressure force, the worst-case drift between static points was 21 lb: nearly as large as the difference between rotor-on and rotor-off data at maximum airspeed (Fig. C1). The difference at maximum airspeed is barely twice the difference between runs near q=50 lb/ft^2, and far less than the uncertainty in balance normal force measurement (Table 2). The maximum difference is also less than the scatter at zero airspeed with the rotor off. The change in pressure force is even less at helicopter-mode rotor speed (Fig. C2).

It might be possible to improve the data for each run by adjusting the spinner pressure data to match NFAC barometric pressure at the static points, with interpolated corrections in between. At best, however, there would result a linear trend of pressure force vs. q with total magnitude less than the uncertainty in Table 2.

For these reasons, it is recommended that no corrections for spinner pressure be applied to the rotor thrust data. No claim is here made that spinner pressure is negligible, only that the available data are too inconsistent to reliably determine the effect, if any, of spinner pressure on the measurement of rotor thrust.

Should a future rotor test on the TTR require more accurate measurement of rotor thrust, or if a different spinner or other change should raise the possibility of greater sensitivity to spinner pressure, improved instrumentation would be in order. In particular, care should be taken to ensure that pressure transducers are fully compensated for temperature. Additional transducers to check for pressure and temperature gradients within the forward cowling are also recommended.

REFERENCES

1. Acree C. W., Jr., and Sheikman, A. L., "Development and Initial Testing of the Tiltrotor Test Rig." American Helicopter Society 74th Annual Forum, Phoenix, AZ, May 14-17, 2018.

2. Russell, C. R., and Acree, C. W., "Modal Test and Analysis of the NASA Tiltrotor Test Rig," American Helicopter Society Technical Conference on Aeromechanics Design for Transformative Vertical Lift, San Francisco, CA, January 16-19, 2018.

3. Acree, C. W., Jr., and Sheikman, A. L., and Norman, T. R., "High-Speed Wind Tunnel Tests of a Full-Scale Proprotor on the Tiltrotor Test Rig." Vertical Flight Society 75th Annual Forum Proceedings, Philadelphia, PA, May 2019.

4. Schatzman, N. L. and Malpica, C., "Acoustic Testing of the Tiltrotor Test Rig in the National Full-Scale Aerodynamics Complex 40- by 80-Foot Wind Tunnel," Vertical Flight Society 75th Annual Forum Proceedings, Philadelphia, PA, May 2019.

5. Bell Helicopter Company: Advancement of Proprotor Technology. Task II – Wind-Tunnel Test Results. NASA CR-114363, Bell Report 300-099-004, Sept. 1971.

6. Seifert, J., "A review of the Magnus effect in aeronautics," Progress in Aerospace Sciences 55 (2012).

7. "Normal distribution," https://en.wikipedia.org/wiki/Normal_distribution, accessed May 2020.